Effects of Ni doping at Co-site on dielectric, impedance spectroscopy and AC-conductivity in La$_2$CoMnO$_6$ double perovskites

Sananda Das[1] · R. C. Sahoo[2] · Shubhankar Mishra[3] · Dipten Bhattacharya[4] · T. K. Nath[1]

Abstract

Multifunctionalities of double perovskites depend strictly on the *3d/4d/5d*-transition metals that can be purposefully tuned by doping effect at the transition metal-site. In the present study, the effects of Ni doping at the Co-site on the dielectric, magnetodielectric, complex impedance, complex modulus and ac-conductivity are investigated in detail for the La$_2$Co$_{1-x}$Ni$_x$MnO$_6$ ($x = 0$, 0.1, 0.5) double perovskites. At room temperature, all the compounds exhibited monoclinic crystal symmetry (space group P2$_1$/n). No structural phase transition and/or impurity phases were observed after doping. The dielectric behavior is investigated over a wide frequency (100–1 MHz) and temperature (100–300 K) ranges, revealing an enhancement in the dielectric constant for the doped samples compared to parent La$_2$CoMnO$_6$. The magnetodielectric effect is also observed for $x = 0$ and $x = 0.1$ samples under 3 T magnetic field. The contributions of grain and grain boundaries at high and low frequencies become evident from the complex impedance spectroscopic and modulus studies. The corresponding carrier activation energies for all the samples are estimated from the Arrhenius fittings. The Nyquist plots are fitted well with an equivalent circuit consisting of two parallel resistance–capacitance elements connected in series, representing the grain and grain boundary effects. The behaviour of the temperature-dependent unitless exponent function predicts the Overlapping Large Polaron Tunneling mechanism in the parent system, while the non-overlapping Small Polaron Tunneling model best describes the doped $x = 0.5$ system. We confirmed by dc-conductivity study that the samples exhibited semiconductor-like nature in a wide temperature range. By revealing the dielectric, impedance and conductivity behaviours of Ni-doped La$_2$CoMnO$_6$, our study broadens the scope of further research on the doping effect at transition metal-sites in perovskites.

Keywords Double perovskite · Dielectric behavior · Impedance spectroscopy · Polaron · AC-conductivity · Semiconductor

1 Introduction

Dielectric materials, whose dielectric properties depend on poor conductivity and electrical polarization, are suitable for practical device applications, when dielectric effects occur close to room temperature [1, 2]. Furthermore, these materials become more attractive when such effects are purposefully tuned by external stimuli, such as electric/magnetic fields or doping. However, these materials are rare in practice [3, 4]. Among these existing rare materials, double perovskite (DP) systems are promising candidates to fulfil the deficiency in this research area.

Moreover, DPs have been the subject of significant research interest for nearly three decades. These are mineral oxide systems with the formula A$_2$BB′O$_6$, where A is a lanthanide (A = La, Sm, Gd) element and B and B' are *3d/4d/5d* transition metal (B/B' = Co, Cr, Mn, Ni) elements. Recent years have seen an enormous rise in the investigation of numerous exciting and stimulating physical properties of various such three-dimensional (3D) DPs [5–8]. Such systems have proven to be desirable candidates for applications related to piezoelectric actuators,

✉ T. K. Nath
  tapnath@gmail.com

1. Department of Physics, Indian Institute of Technology, Kharagpur 721302, India

2. School of Materials and Chemical Technology, Tokyo Institute of Technology, 2-12-1 Ookayama, Meguro-ku, Tokyo 152-8552, Japan

3. School of Materials Science and Nanotechnology, Jadavpur University, Calcutta 700032, India

4. Advanced Materials and Chemical Characterization Division, CSIR-Central Glass and Ceramic Research Institute, Calcutta 700032, India

transducers, sensors, half-metallics and photocatalytic activity, thus demanding significant research attention [9–12].

Extensive literature has been published on Ln_2CoMnO_6 DPs based on the lanthanide series (Ln = Sm, La, Y, Gd) [13, 14]. One such interesting DPs from this family, La_2CoMnO_6 (LCMO), has significant technological contributions; and has been extensively studied by researchers due to its low cost and unique electric dipolar orderings, electrical and magnetic properties [6, 14–17]. It has been reported that the LCMO system has, in addition to its insulating behaviour, a ferromagnetic ordering temperature of ~ 225 K [18]. This system exhibits suitable dielectric and magnetodielectric properties in several structures, such as thin films, single crystals and polycrystalline forms [19, 20]. The dielectric behaviour of LCMO was in focus of several research groups due to its high scientific and technological importance [21].

In addition, numerous researchers have focused on exploring the dielectric, magneto-dielectric, complex impedance spectroscopic, and ac-conductivity behavior of $3d$ transition metals (Mn, Fe, Co, Ni, Cr) doped at the B site of single and double perovskite systems [22, 23]. Attempts have been made to modulate the B-site cation ordering and thus tune the physical properties of LCMO. Among the magnetic metals, Ni is a crucial dopant which, when doped at the B-site, may aid in tuning the bond angles (B−O−B′) and bond lengths (B−O, B′−O) so that it may help to achieve unique spontaneous magnetic and electric dipolar properties due to changes in the band structure [24, 25]. Doping-driven B-site disorder may also help to modulate the grain and grain boundary effects. Different relaxation processes have been observed in perovskite ceramics, resulting from the various defects/oxygen vacancies due to doping effects [26, 27]. An extensive literature survey shows that no systematic research has been carried out to date that investigated Ni-doping at the Co site of LCMO. We chose Ni doping at the Co site, because individually, they exhibit interesting dielectric properties when interacting with Mn ions [5, 14, 15]. Therefore, it is important to study partial doping effect by Ni at Co site on dielectric properties in such DPs.

In this work, we have focused on the effects of the substitution of Ni ions (10% and 50%) at the 100% Co ion site on the structural, dielectric, magnetodielectric, modulus, ac-conductivity, and complex impedance properties in LCMO and their comparative analysis over broad temperature and frequency ranges. The dielectric and impedance properties show improvement with Ni doping compared to parent LCMO. We discuss the essential role played by the doping in the form of disorder/defects in interrelating these dielectric properties. We confirmed that grain and grain boundary effects also play a crucial role for these diverse properties. This offers an interesting way to engineer dielectric systems for better performance.

2 Experimental details

The polycrystalline $La_2Co_{1-x}Ni_xMnO_6$ ($x = 0$ (LCMO), $x = 0.1$ (LCNMO_0.1, 0.9), $x = 0.5$ (LCNMO_0.5, 0.5)) samples are synthesized by the standard sol–gel synthesis method from stoichiometric mixture, where high purity chemical reagents La_2O_3 (Sigma-Aldrich, ≥ 99.9%) $Co(NO_3)_2.6H_2O$ (Merck, ≥ 98.0%), $Ni(NO_3)_2.6H_2O$ (Loba, ≥ 98.0%) and $(CH_3COO)_2Mn \cdot 4H_2O$ (Merck, ≥ 99.5%) were used as the primary raw materials [14]. A stoichiometric amount of La_2O_3 is dissolved in HNO_3, forming $La(NO_3)_3$ with the subsequent dissolution of other stoichiometric compounds in deionized water to get clear solutions. Next, all the solutions are mixed by continuous stirring and citric acid $C_6H_8O_7 \cdot H_2O$ is added as a chelating agent to ensure that the total volume of solution ratio results in 1:1.5, making a viscous solution. Finally, this clear solution is heated at a temperature of 150 °C for 72 h with the help of a microprocessor-controlled hot plate. The obtained precursor is then calcinated at 1200 °C for 10 h to reach bulk polycrystalline powder. This calcined powder is then pelletized utilizing a hydraulic pressure and is sintered at 1250 °C for 6 h.

We performed the phase analysis of the samples with a Bruker powder X-ray Diffractometer (XRD) with Cu-Kα radiation ($\lambda = 1.542$ Å), and a Merlin FESEM microscope was used to estimate the grain size. Dielectric, magnetodielectric and impedance measurements are carried out with a Hioki LCR HiTester 3532-50 impedance analyser meter for a temperature range of 100–300 K at various frequencies mentioned below.

3 Results and discussion

3.1 Structural characterization

In Fig. 1a–c, we show the room temperature X-ray diffraction (HR-XRD) data of the LCMO, LCNMO_0.1,0.9, and LCNMO_0.5,0.5 samples, which clearly show the perovskite type structure and polycrystalline nature of the samples. The observed XRD peaks are sharp, suggesting that our systems are polycrystalline bulk [28]. For the structural information, Rietveld refinements are performed with FULLPROF software, which affirms a single pure phase for all our synthesized samples. The X-ray diffraction peaks of all the samples correspond to the monoclinic crystal structure, and the refinement data appropriately fits the $P2_1/n$ space group. This observation is in agreement with the results published earlier [14]. The refined structural parameters, such as cell parameters and unit
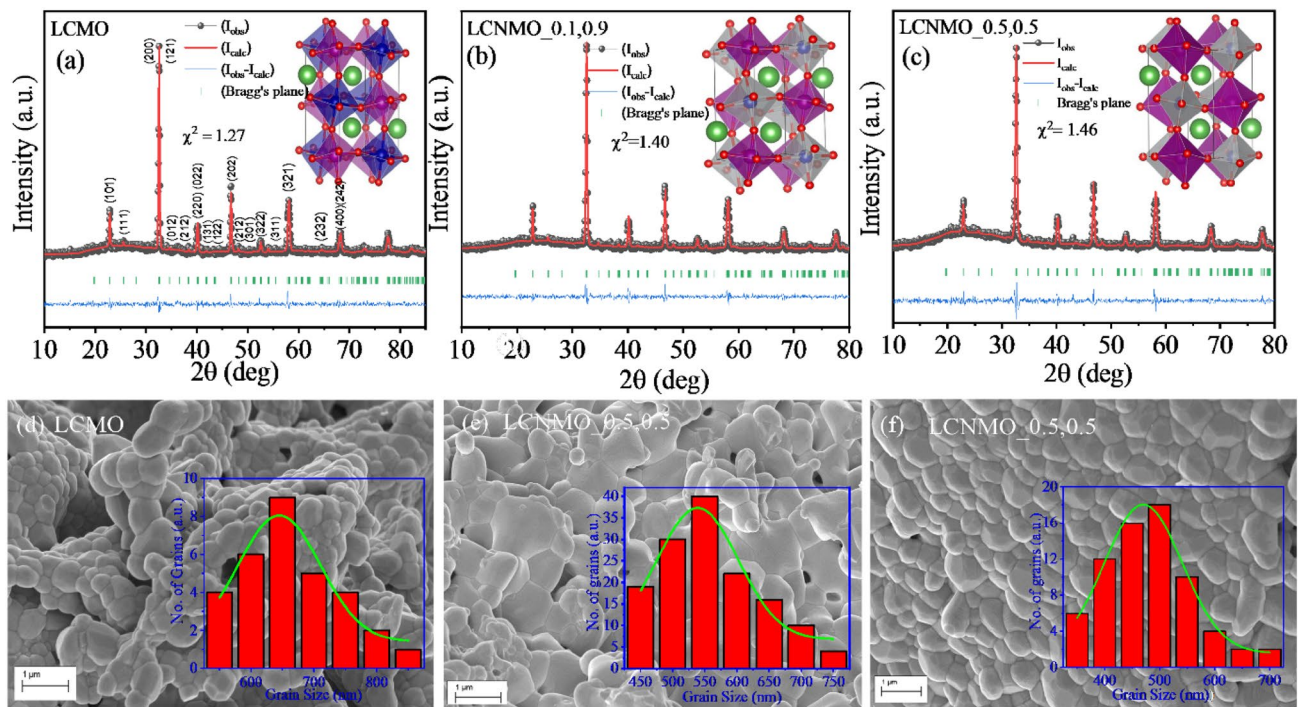
Fig. 1 Rietveld refinement of XRD data collected at RT for **a** LCMO, **b** LCNMO_0.1, 0.9 and **c** LCNMO_0.5, 0.5 samples and the insets of the respective figures illustrates the local unit cell of corresponding crystal structure. The SEM micrograph images and the insets show histograms of grain size obtained from SEM micrographs for **d** LCMO, **e** LCNMO_0.1, 0.9 and **f** LCNMO_0.5, 0.5 samples

Table 1 Refined structural parameters after Rietveld refinement for HRXRD data for $La_2Co_{1-x}Ni_xMnO_6$ ($x = 0.0, 0.1, 0.5$) double perovskite systems at room temperature

x	0	0.1	0.5
Phase (space group)	Monoclinic $(P2_1/n)$	Monoclinic $(P2_1/n)$	Monoclinic $(P2_1/n)$
t	0.833	0.830	0.822
a (Å)	5.498 (9)	5.504 (9)	5.497 (4)
b (Å)	5.494 (4)	5.485 (4)	5.477 (2)
c (Å)	7.789 (2)	7.795 (3)	7.783 (6)
β°	89.66(8)	89.70 (9)	89.70 (6)
V (Å³)	235.33 (6)	235.39 (2)	234.36 (8)
χ^2	1.27	1.40	1.46

Table 2 Bond distances and bond angles for $La_2Co_{1-x}Ni_xMnO_6$ ($x = 0$, 0.1, 0.5) double perovskite systems at room temperature

x	0	0.1	0.5
Mn–O1(Å)	1.951	1.844	2.145
Mn–O2(Å)	1.790	1.863	1.918
Mn–O3(Å)	1.923	1.872	1.936
Ni/Co–O1(Å)	1.994	2.115	1.811
Ni/Co–O2(Å)	2.138	2.085	2.063
Ni/Co–O3(Å)	2.009	2.065	1.888
Mn–O1–Co/Ni	160.159°	157.724°	157.221°
Mn–O2–Co/Ni	163.158°	159.375°	154.044°
Mn–O3–Co/Ni	164.003°	163.659°	158.891°

cell volumes, obtained for all studied samples, are listed in Table 1. Interestingly, it is observed that the unit cell volume of LCNMO_0.1, 0.9 is higher than the unit cell volume of LCMO and LCNMO_0.5,0.5. Since, Ni^{2+} ions have smaller ionic radii than Co^{2+} ions, it is normal for the unit cell volume to decrease with doping. However, this is not the case for our LCNMO_0.1,0.9 sample. This increase in unit cell volume may be attributed to the presence of oxygen vacancies in the LCNMO_0.1, 0.9 sample [29]. From Table 2, it is observed that the Mn–O1 and Mn–O3 bond lengths first decrease and then increase with

Ni doping, whereas the Mn–O2 bond length increases with doping. The Ni/Co–O1, Ni/Co–O2 and Ni/Co–O3 bond lengths follow a reverse trend. The values of the bond angles (Mn–O–Co/Ni) also decrease with Ni doping. With the help of the software Visualization of Electronic and Structural Analysis (VESTA), the structural parameters of the local environment of the octahedral coordination of Co(Ni)/Mn ions with oxygen, bond angles and bond lengths are obtained and are shown in Table 2. No systematic changes are obtained in the doped DPs, suggesting that partial disorder is achieved after Ni doping. The local

crystal structures of the respective samples are shown in the insets of Fig. 1a–c, where two $LaBO_3$ (i.e., La(Co/Ni)O_3 and LaMnO$_3$) perovskite structures are periodically arranged uniformly to form a DP unit cell, and the (Co/Ni)O$_6$ and MnO$_6$ octahedra alternate at the corners of this unit cell. The Rietveld analysis concludes that the $3d$ transition metals ((Co/Ni)/Mn) can occupy specific positions, *i.e.*, Co/Ni occupies 2c (0, ½, 0) and Mn occupies 2d (½, 0, 0) positions along all the crystallographic axis in our samples. In addition, the literature review suggested that, if Goldschmidt tolerance factor (t) < 0.97, the compound becomes either monoclinic (P2$_1$/n) or orthorhombic [30] and deviation from this designated value also indicates disorder in the samples [31]. The t values calculated from formula [32]:

$$t = \frac{2(r_A + r_O)}{\sqrt{2}(r_B + r_{B'} + 2r_O)},$$

Table 3 Activation energies and relaxation times for La$_2$Co$_{1-x}$Ni$_x$MnO$_6$ ($x = 0.0, 0.1, 0.5$)

x	0	0.1	0.5
E_a (eV)	0.060	0.101	0.105
τ_s (s)	8.832×10^{-7}	8.694×10^{-8}	7.072×10^{-8}

are 0.833, 0.830 and 0.822 for LCMO, LCNMO_0.1,0.9 and LCNMO_0.5,0.5 systems (where r_A, r_B and $r_{B'}$ are the ionic radius of the A, B and B′-site cations, respectively, and r_O is the ionic radius of the anion), respectively. Therefore, all the structural information confirms the presence of disorder in our investigated systems.

The FESEM micrographs, as shown in Fig. 1d–f, depict the non-uniform distribution of grains separated by grain boundaries. As evaluated from the histograms, the average grain size range for all of our prepared samples is between 500 and 650 nm, indicating their bulk nature.

3.2 Dielectric study

To investigate the dielectric behaviour and frequency-dependent dielectric relaxations of the systems, the real part of the dielectric constant (ε′) is measured in the frequency range of 100 Hz–1 MHz at different temperatures from 100 K to 240 K and the plots are shown in Fig. 2a–c. It is well-known that any dielectric material comprises highly conducting grains and relatively poor conducting grain-boundaries [33]. Here, the ε′ value is large at low-frequency regime. Such a large value is observed because of the build-up of charges under the ac electric field, which results in an interfacial polarization [34, 35]. Moreover, the electric charges do not follow the electric field oscillations at higher frequencies, producing decreased ε′ values in the
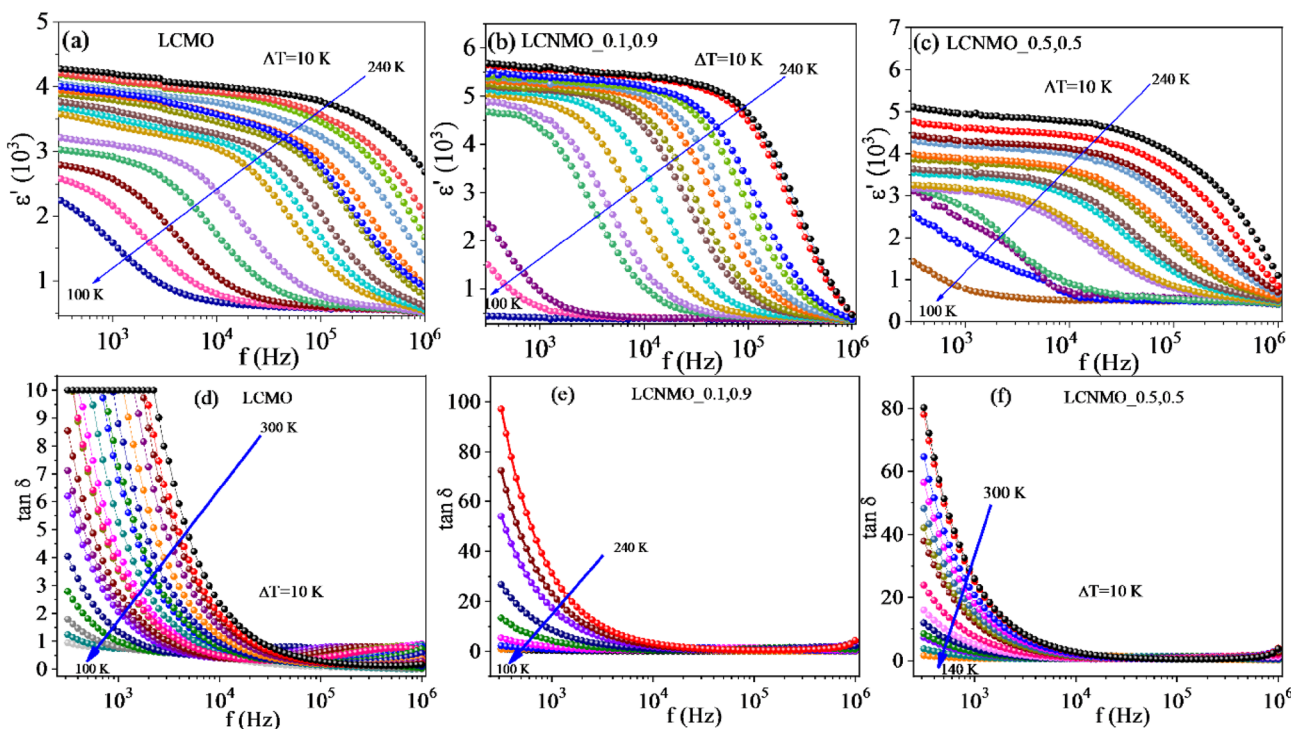

Fig. 2 Frequency-dependent ε′ at different temperatures for **a** LCMO, **b** LCNMO_0.1, 0.9 and **c** LCNMO_0.5, 0.5 samples. The frequency variation of tan δ loss of **d** LCMO, **e** LCNMO_0.1, 0.9 and **f**LCNMO_0.5, 0.5 samples

high-frequency range [36]. Besides, the mid-frequency and high-frequency plateau regions in ε″ curves indicate that the studied systems are electrically inhomogeneous [37]. In addition, it suggests that only intrinsic effects are responsible for the dielectric relaxation in the higher frequency region, and the extrinsic origin of grain-boundary or Maxwell–Wagner interfacial polarization contributes to the lower frequency regime, as suggested in refs. [38, 39]. However, in the low-frequency regime, the ε′ value rises with increasing temperature and eventually decreases and merges at higher frequencies.

Figure 2a–c reveals that LCNMO_0.1, 0.9 and LCNMO_0.5, 0.5 samples show an improvement in the value (~ 5653 and ~ 5000 at a frequency of 1 kHz, respectively) of ε′ as compared to LCMO (~ 4222) at 240 K. This increase in ε′ may occur due to Ni-doping at the Co site, resulting in inhomogeneity between the grain and grain boundary regions and/or disorder in the crystal structure and/or vacancies. The loss tangent factor is also measured for all the systems and it is observed to decrease with increasing frequency, as shown in Fig. 2d–f. The loss is higher in the doped samples than in the parent compound, indicating oxygen vacancy concentration increased by doping.

The real parts of the temperature-dependent dielectric permittivity ε′ and loss tangent factor for different frequencies (500 Hz–1 MHz) are shown in Fig. 3a–f. All the samples show a very large value of ε′ in the temperature range of 250–300 K at lower frequencies. Interestingly, near room temperature, LCNMO_0.1, 0.9 and LCNMO_0.5, 0.5 exhibit a large dielectric value of ~ 5826 and ~ 5821, respectively, compared to parent compound LCMO (~ 4595) at 1 kHz. However, with decreasing temperature, the ε′ values decrease and then experience a frequency-dependent sharp drop. Again, at very low temperatures (i.e., below 50 K for LCMO and LCNMO_0.1, 0.9), the values of ε′ show evidence of saturation with no dispersion regardless of the applied frequency. This observed behaviour is intrinsic to the systems. The ε′ value increases with increasing temperature due to Maxwell–Wagner-type contribution to the permittivity originating from enhanced conductivity and consistent with the frequency dependent ε′ [34, 40]. The high values of ε′ at high temperature regime and low frequencies in LCNMO_0.1, 0.9 and LCNMO_0.5, 0.5 systems compared to LCMO may be associated with the influence of disorder on the local potential fluctuations and accumulation of more charges at the grain boundaries giving rise to higher space charge polarization [41]. Furthermore, the tan δ loss curves (Fig. 3d–f) show broad peaks that move to higher temperatures with frequency increase. This shift suggests a thermally activated relaxor-like behaviour in our samples, which may be a contribution of relaxation time crossover associated with the grains and grain boundaries [42, 43]. In addition, the low-frequency dielectric loss in the doped samples is little higher as compared to the parent compound.
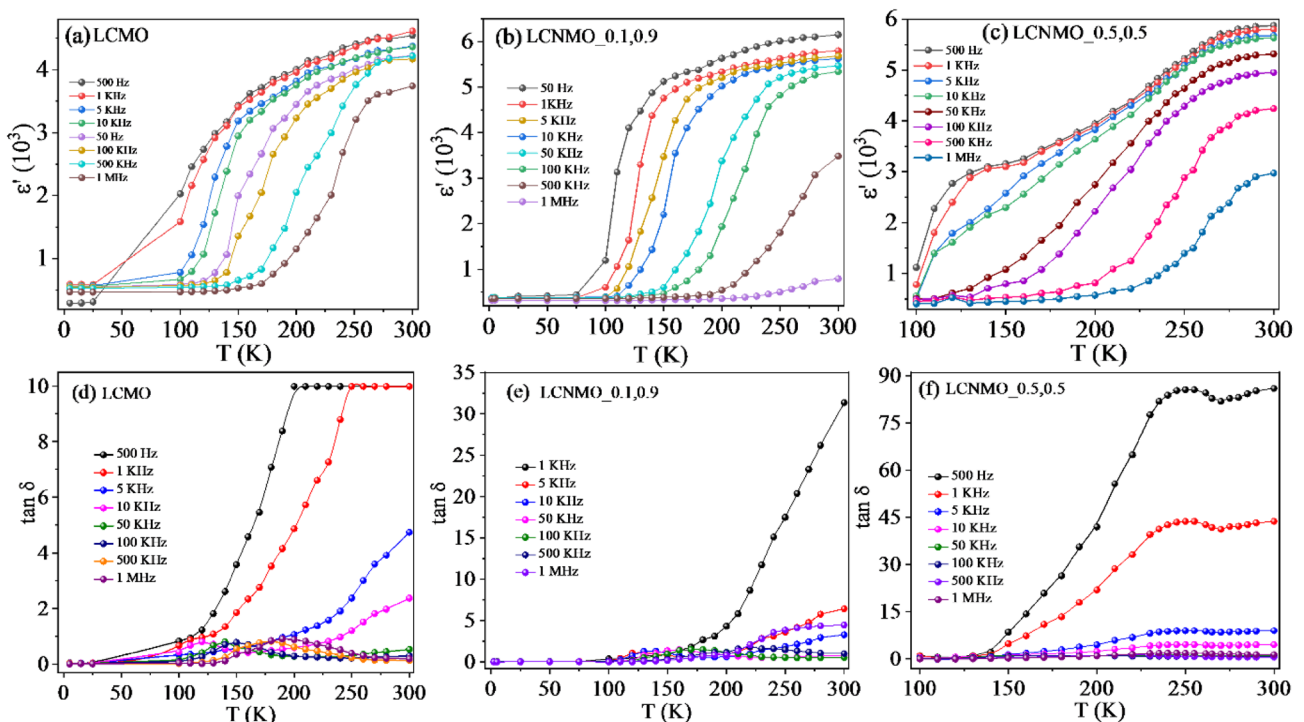

Fig. 3 Variation of ε′ with temperature at different frequencies for **a** LCMO, **b** LCNMO_0.1, 0.9 and **c** LCNMO_0.5, 0.5 samples. Variation of tan δ loss with temperature at different frequencies for **d** LCMO, **e** LCNMO_0.1, 0.9 and **f** LCNMO_0.5, 0.5 samples

The imaginary part of dielectric constant (ε'') has been plotted as a function of temperature for all the three samples at different frequencies (Fig. 4a–c). LCMO and LCNMO_0.1, 0.9 samples show relaxor-like behaviour around 150 K. The relaxation peak position shifts to higher temperatures as frequency increases. However, no prominent relaxation peak is spotted for LCNMO_0.5, 0.5 sample for the given temperature range. A large separation in temperature is observed between the tan δ and ε'' peaks in Fig. 4d, e for LCMO and LCNMO_0.1, 0.9 samples. Hence, we can say that no permanent dipoles exist in both the samples. This may be due to the relaxation time crossover concerning the grain and grain boundaries [44]. The Arrhenius relation for relaxation mechanism is given by [45]

$$\tau^\varepsilon = \tau_0^\varepsilon exp \frac{E_a^\varepsilon}{k_B T},$$

where E_a^ε is the activation energy for the relaxation process and τ_0^ε is the pre-exponential factor. By fitting $\ln \tau^\varepsilon$ vs. $1/T$ plots (shown in insets of Fig. 4a, b), the obtained activation energies and relaxation times are 0.132 eV, 0.091 eV and 1.943×10^{-10} s, 1.674×10^{-8} s for the LCMO and LCNMO_0.1, 0.9 samples, respectively.

The Magnetodielectric (MD) effect, which depends on the external magnetic field, holds considerable attention for device applications using a particular material. Therefore, the MD effect was measured in the samples under study. The temperature-dependent MD effect measurements under 3 T field are shown in Fig. 5a–c. They show improved magnetodielectricity above 200 K in doped samples compared to parent. Moreover, a clear anomaly is observed for both LCMO and LCNMO_0.1, 0.9 at ~210 K and ~242 K at a frequency of 100 kHz. These temperatures are close to the magnetic ordering temperatures suggested in Ref. [46] and they give evidence of the MD behavior in our systems. Such behaviour may be attributed to the intrinsic magnetoelectric coupling in multiferroics [5, 47]. Surprisingly, no such anomaly is observed for the LCNMO_0.5, 0.5 sample, since the data recorded in the presence of 3 T falls precisely on the 0 T curve. This result may be the consequence of the applied magnetic field not being sufficiently large enough to produce the required MD effect.

3.3 Complex impedance spectroscopic study

Examining complex plane experimental data is a powerful approach to interpret the contributions of grain, grain-boundary, and sample-electrode interface towards the dielectric properties in electronically inhomogeneous materials [48]. It is known that impedance can be written as $Z^* = Z' - jZ''$, where Z' ($Z' = R/[1 + (\omega RC)^2]$) and Z'' ($Z'' = \omega R^2 C/[1 + (\omega RC)^2]$) are the real and imaginary parts
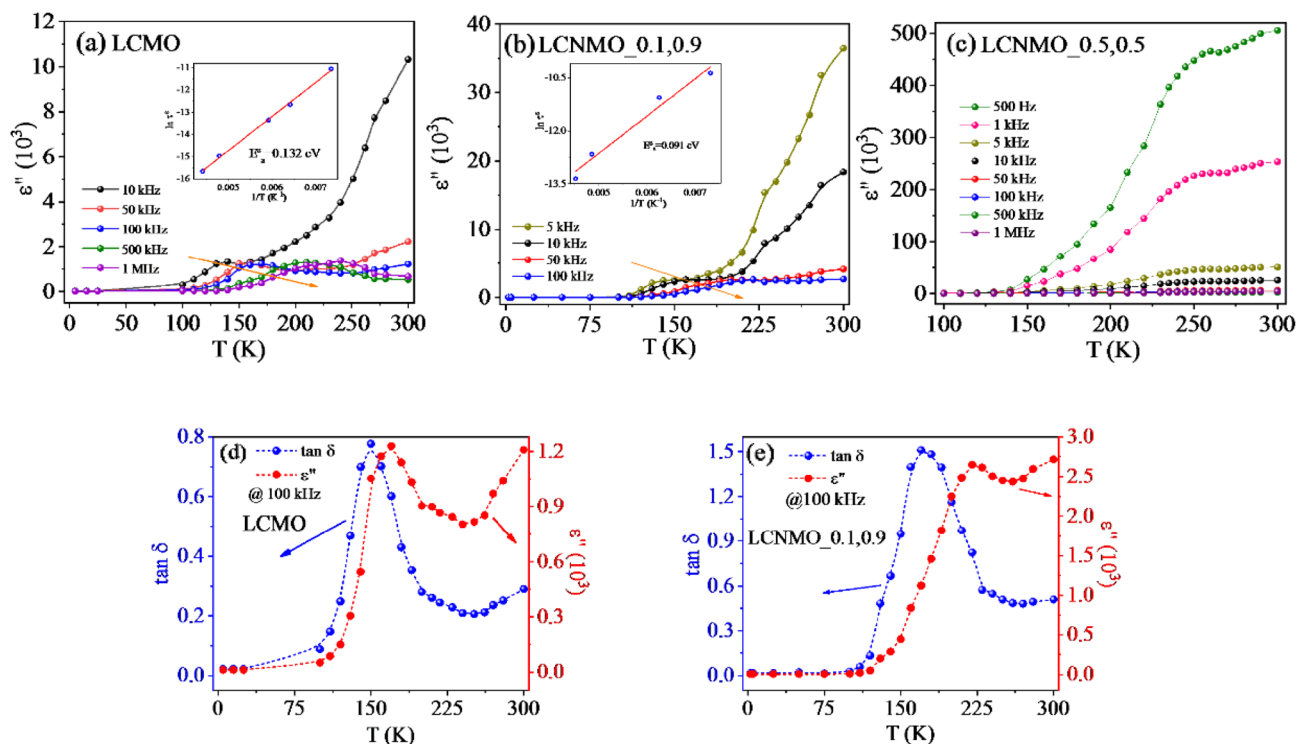

Fig. 4 Variation of ε'' with temperature at different frequencies for **a** LCMO, **b** LCNMO_0.1, 0.9 and **c** LCNMO_0.5, 0.5 samples
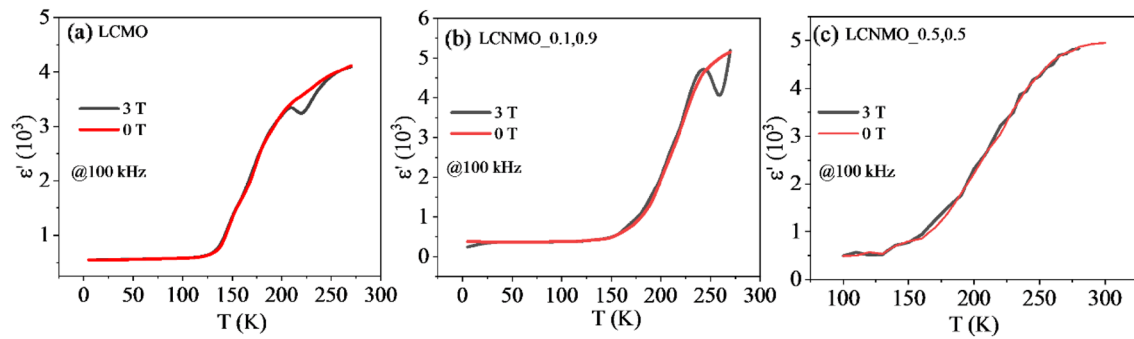
Fig. 5 Variation of dielectric behaviour at 100 kHz for 0 and 3 T magnetic field for **a** LCMO, **b** LCNMO_0.1, 0.9 and **c** LCNMO_0.5, 0.5 samples
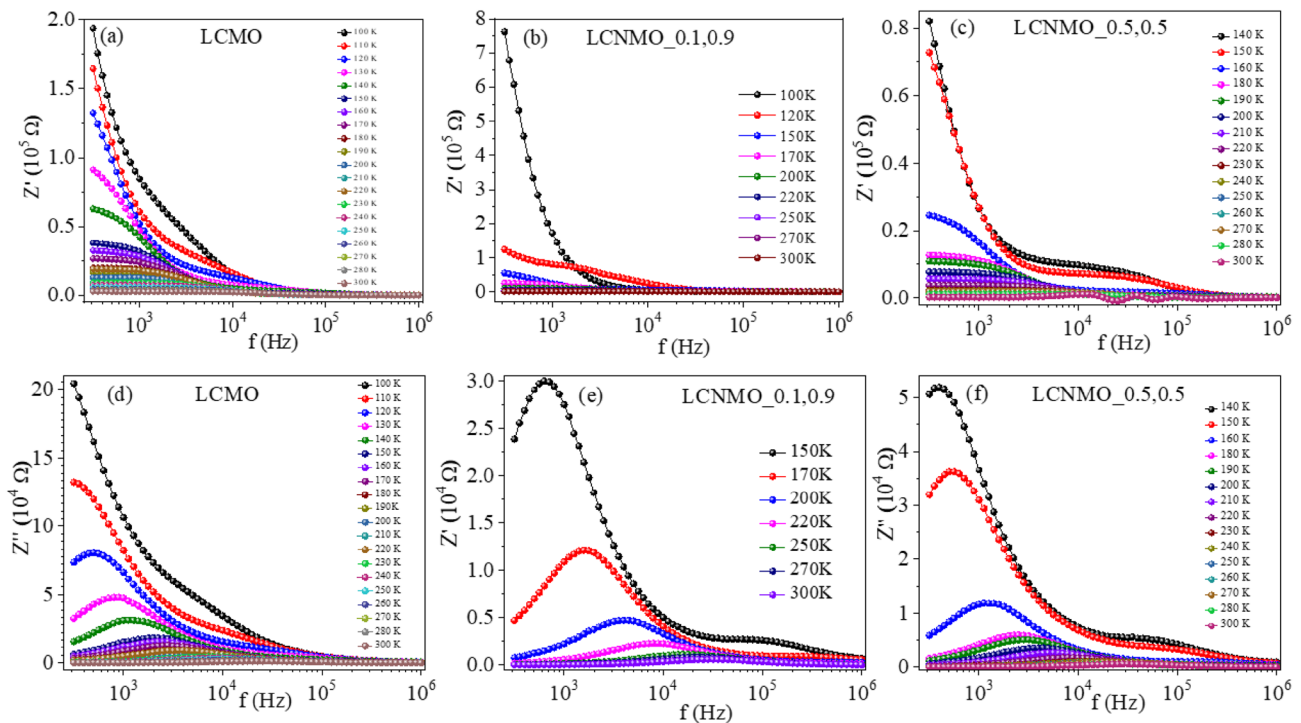

Fig. 6 Temperature dependent Z′ variation as a function of frequency for **a** LCMO, **b** LCNMO_0.1,0.9 and **c** LCNMO_0.5, 0.5 samples. Temperature dependent Z″ variation with frequency for **d** LCMO, **e** LCNMO_0.1, 0.9 and **f** LCNMO_0.5, 0.5 samples

of impedances, respectively. In case where long-range conduction processes are present, Z* is more convenient for the resistive and/or conductive analysis. Figure 6a–f shows the variations of Z′ and Z″ with respect to frequency for LCMO, LCNMO_0.1, 0.9 and LCNMO_0.5, 0.5 at different temperatures. It is observed that, with increasing frequency, the magnitude of Z′ decreases. This decrease is a direct indication of increased ac conductivity and lower resistances of grains and grain boundaries in these samples [49]. In addition, the decrease in Z′ with increasing temperature in the lower frequency regime signifies negative temperature coefficient of resistance behavior, as

suggested in Ref. [50]. The Z′ values merge in the high-frequency region (> 100 kHz) regardless of the temperature change. This nature may be attributed to the discharge of space charges. In addition, it is observed that the Z′ plateau shifts with increasing frequency and temperature. This nature in Z′ curves, along with the enhancement in the ac conductivity with increasing temperature and frequency, support single relaxation mechanism in these samples. The Z′ value is lower in case of LCNMO_0.5, 0.5 compared to the other samples which indicate that the conductivity is higher in this sample compared to LCMO and LCNMO_0.1, 0.9.

The peak positions in Z″ curves shift to higher frequencies with an increase in temperature (Fig. 6d–f), indicating the existence and change of the relaxation process in all three samples [50]. The broadening of the peaks with temperature indicates the temperature-dependent relaxation, and the relaxation time distribution depends on different relaxation processes. A possible explanation for such an effect in the materials can be defects or vacancies arising due to the space charges at higher temperatures, whereas electrons or immobile species—at low temperatures. However, the asymmetric broadening of these peaks indicates the deviation from the ideal Debye behaviour and increased relaxation time. Moreover, the magnitude of Z″ decreases with the peak shift towards the higher frequencies that, in turn, merges in the high-frequency region. This behaviour demonstrates that space charge polarization is strongly active at lower frequencies and less active at higher frequencies [50]. Furthermore, the Z″ values of the LCNMO_0.5, 0.5 sample is higher than the other samples indicating higher energy storage capacity for this sample compared to others.

The most probable relaxation time τ ($= 1/2\pi f_r$) in such systems can be calculated from the positions of the peaks in the Z″ vs. log(f) plots. Here, f_r is the relaxation frequency, i.e., the frequency at which Z″ is found to be maximum. It follows Arrhenius′ law as

$$\tau = \tau_0 exp\frac{E_a}{k_B T},$$

where τ_0 is the pre-exponential factor, E_a the activation energy, k_B the Boltzmann constant and T is the absolute temperature. The grain and grain boundary activation energies for all the studied samples are estimated from the slopes of the log(τ) vs. $1/T$ curves, as shown in Fig. 7a–c. The E_a values related to grain boundary for LCMO, LCNMO_0.1, 0.9 and LCNMO_0.5, 0.5 are found out to be 0.060, 0.101 and 0.105 eV, respectively (Fig. 7a–c). The relaxation times are also calculated, and those are 8.832×10^{-7}, 8.694×10^{-8}, and 7.072×10^{-8} s, respectively (Table 3). Again, the E_a values linked with grain for LCMO, LCNMO_0.1, 0.9 and LCNMO_0.5, 0.5 are estimated as equal to 0.060, 0.154 and 0.105 eV. The relaxation times, in this case, are 8.832×10^{-7}, 7.803×10^{-12}, and 4.617×10^{-10} s, respectively. It is known that $E_a > 1$ eV is assigned to the ionic conduction and < 1 eV to small polaronic hopping [51]. Here, the obtained activation energies have a good resemblance to the polaron activation energies and correspond to the n-type polaron hopping found in similar perovskite compounds [52, 53]. Moreover, the relaxation times associated with the grain boundary are almost four orders higher than that of grain for LCNMO_0.1, 0.9 and two orders higher for LCNMO_0.5, 0.5, suggesting that the charge carriers at the grain boundaries have
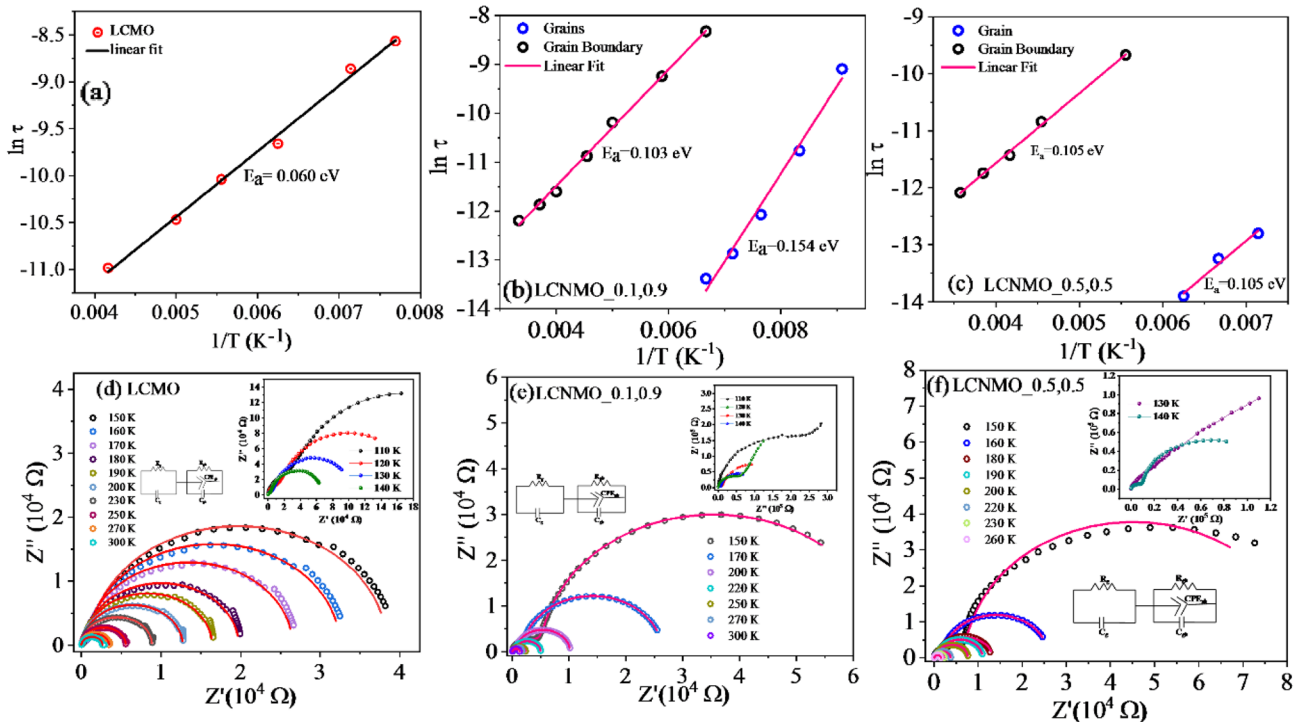

Fig. 7 Activation energies for **a** LCMO, **b** LCNMO_0.1, 0.9 and **c** LCNMO_0.5, 0.5 samples. Nyquist plots (Z″ vs. Z′) for **d** LCMO, **e** LCNMO_0.1, 0.9 and **f** LCNMO_0.5, 0.5 samples at various temperatures

Table 4 Grain and grain boundary resistance and capacitance for $La_2Co_{1-x}Ni_xMnO_6$ ($x = 0.0$, 0.1, 0.5). The fitted parameters for LCMO, LCNMO_0.1, 0.9, LCNMO_0.5, 0.5 samples are shown below in sequence

T (K)	$R_g (\Omega)$	$R_{gb} \times 10^3 (\Omega)$	$C_g \times 10^{-10}$ (F)	$C_{gb} \times 10^{-10}$ (F)
150	11,190.0	41.785	4.435	1.896
160	8043.1	31.600	4.593	1.920
170	568.6	23.559	4.838	1.947
180	315.1	19.420	5.573	2.000
190	225.4	16.180	6.279	2.046
200	139.3	12.580	7.847	2.111
230	82.8	8.800	10.350	2.219
250	27.3	5.537	3.910	2.342
270	13.4	3.485	7.320×10^{-6}	2.436
300	10.5	2.645	9.439×10^{-10}	2.473
T (K)	$R_g (\Omega)$	$R_{gb} \times 10^3 (\Omega)$	$C_g \times 10^{-10}$ (F)	$C_{gb} \times 10^{-10}$ (F)
150	4676.0	58.920	2.527	4.034
170	1637.0	24.240	2.477	4.115
200	553.2	9.544	1.003×10^{-7}	4.101
220	300.9	4.642	6.674×10^{-4}	4.142
250	118.4	2.241	6.562×10^{-9}	3.372
270	142.5	2.799	2.799×10^{-9}	2.861
300	64.7	1.214	1.624×10^{-6}	4.308
T (K)	$R_g (\Omega)$	$R_{gb} \times 10^3 (\Omega)$	$C_g \times 10^{-10}$ (F)	$C_{gb} \times 10^{-10}$ (F)
150	7723.0	75.210	1.606	3.460
160	3029.0	23.530	3.314	5.422
180	742.5	12.670	3.804	3.744
190	1027.0	10.070	2.880	5.407
200	490.7	7.183	4.900×10^{-8}	5.435
220	300.8	3.460	4.610×10^{-8}	5.489
230	205.4	2.160	9.893×10^{-9}	6.331
260	74.6	1.445	1.660×10^{-9}	5.400

lower mobility than that of grains. The decreasing values of τ with increasing temperature indicate semiconductor-like behaviour as a result of oxygen vacancies in our studied bulk samples.

Figure 7d–f shows the variations of Z′ and Z″ plot (i.e., Nyquist plot) in a complex impedance plane for LCMO, LCNMO_0.1, 0.9, and LCNMO_0.5, 0.5 systems from 150 to 300 K within a frequency range of 100 Hz to 1 MHz. It is observed that, as the temperature rises, the values of impedance decrease sharply. These decreasing values signify a sharp increase in conductivity with an increase in temperature, thus indicating that the systems have semiconducting properties at high temperatures. The incomplete semi-circular arcs are observed at very low temperatures, which start to build up as the temperature increases. Two semi-circular arcs are seen at temperatures between 130 and 170 K in all the samples. A large semi-circular arc at low frequencies indicates the contributions of grain boundaries,

and the small high-frequency arc refers to grains. However, at higher (> 170 K) temperatures, the grain boundary effect dominates as indicated by single semi-circular arcs. There is a slight depression present in the semicircles, which is evidence of the non-Debye type of relaxation effect in our investigated systems. The shift from ideal behaviour can be due to several factors, such as grain size distribution, grain boundary effect, and grain orientation.

With the help of commercially available software ZSIMPWIN Version 3.2.1, the Nyquist plots are fitted with an equivalent circuit consisting of two parallel resistance–capacitance (RC) elements connected in series representing the grain and grain boundary effects (Fig. 7d–f). The grain and grain boundary resistances and capacitances, as estimated from the fitted data, are shown in Table 4. The values of both the grain boundary and grain resistances decrease with an increase in temperature in all our investigated systems, confirming semiconducting behaviour.

Table 5 Activation energies calculated from the ac-conductivity measurements for $La_2Co_{1-x}Ni_xMnO_6$ ($x = 0.0$, 0.1, 0.5)

x	1 kHz	5 kHz	10 kHz	100 kHz
0.0	0.065 eV	0.060 eV	0.107 eV	0.090 eV
0.1	0.106 eV	0.092 eV	0.089 eV	–
0.5	0.084 eV	0.081 eV	0.069 eV	0.054 eV

3.4 Complex modulus study

The complex modulus analysis is a powerful tool to investigate the dynamical aspects of electric transport phenomena, in particular conductivity and relaxation process of the dielectric materials. It confirms the ambiguity arising from the grain or grain boundary effects at high temperatures, which may not be identified from complex impedance measurements. The complex modulus (M*) is suited to comprehend the influence of the localized relaxations in the samples. It is the inverse of the complex permittivity and can be expressed as follows [54]:

$$M^* = \frac{1}{\varepsilon'} = \frac{1}{\varepsilon' - j\varepsilon''} = M' + jM'' = \frac{\varepsilon'}{[\varepsilon'^2 + \varepsilon''^2]} + j\frac{\varepsilon''}{[\varepsilon'^2 + \varepsilon''^2]},$$

where M′ and M″ are real and imaginary parts of M*, respectively. Figure 8a–f depicts the frequency-dependent M′ and M″ parts of M* ($= M' + jM'' = j\omega\varepsilon_0 Z^* = j\omega\varepsilon_0 Z' - \omega\varepsilon_0 Z''$)

at various temperatures [54]. At low temperatures, relaxation peaks are observed in both the high- and low-frequency ranges in the M″ curves, indicating the effect of both grain and grain boundaries. At higher temperatures, a single peak in the low-frequency region indicates grain boundary contribution only. In all samples, the grain peak intensities in the M″ spectra are greater than the grain boundary peaks. This suggests that the capacitance of the grains (C_g) is less than the grain boundary capacitance (C_{gb}) (as shown in Table 4). We can also see that the C_g of LCNMO_0.1, 0.9 and LCNMO_0.5, 0.5 is lower than that of parent material LCMO. This is due to the larger intensity of grain peaks in the modulus spectra of doped systems.

The plots of M″ and Z″ vs. scanned frequency, when combined, provide an understanding of the nature of the movements (long-range or short-range) of the charge carriers. Supplementary Fig. 1a shows the combined plots for the LCMO sample at 180 K. The relaxation at high frequencies, which corresponds to the low value of Z″ and high value of M″, is attributed to the grain contribution. The high value of the Z″ peak and low value of the M″ peak at higher frequencies is assigned to the grain boundary contribution. Similar plots are obtained for the samples LCNMO_0.1, 0.9 and LCNMO_0.5, 0.5 (not shown here). The insets of Fig. 8d–f show the variation of the normalized complex electrical modulus (M″/M″$_{max}$) with normalized frequency (f/f$_{max}$), where f_{max} is the corresponding frequency of the peak position of M″ at M″$_{max}$. The
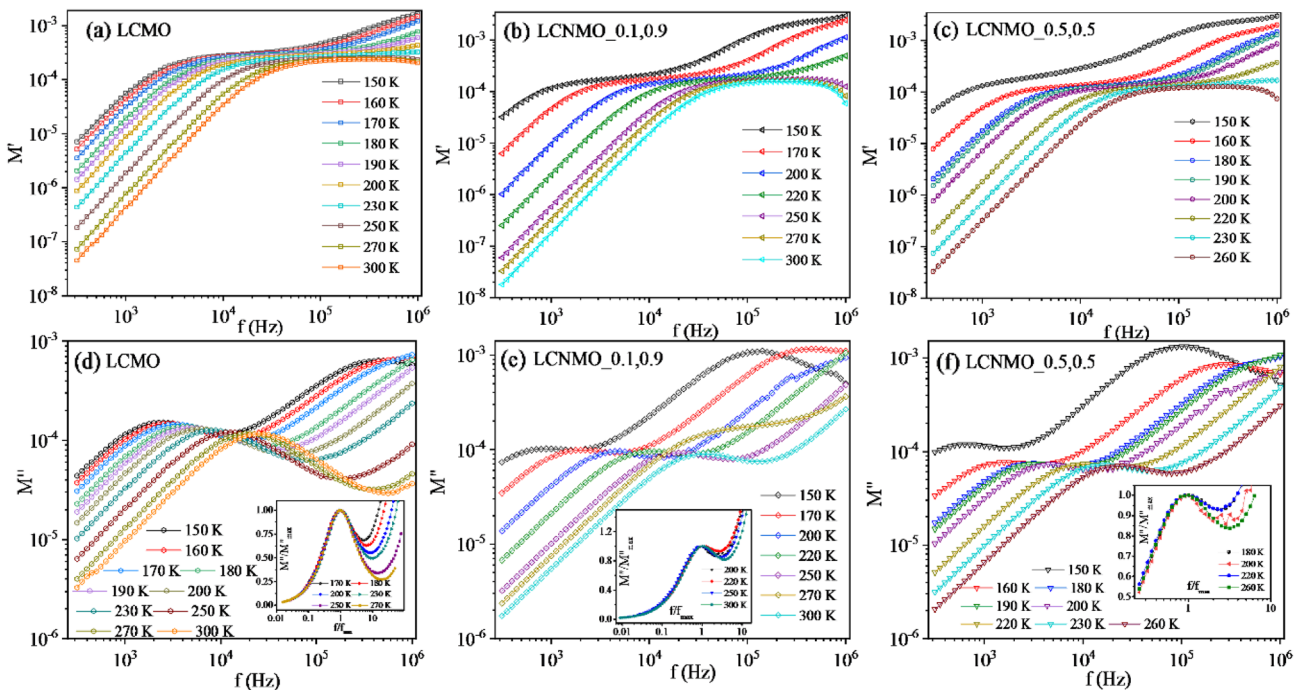

Fig. 8 Temperature-dependent real part of modulus M′ for **a** LCMO, **b** LCNMO_0.1, 0.9 and **c** LCNMO_0.5, 0.5 samples. The temperature-dependent imaginary part of modulus M″ for **d** LCMO, **e** LCNMO_0.1, 0.9 and **f** LCNMO_0.5, 0.5 samples and the insets show the scaling behavior of the modulus

modulus spectra at various temperatures overlap and scale into a single master curve. This portrays the presence of similar relaxation mechanisms at different temperatures in all our investigated systems. However, a wide gap between M''/M''_{max} and Z''/Z''_{max} peak (shown only for LCMO in Supplementary Fig. 1c) portrays the non-Debye type of behaviour. In the entire range of observed temperature, the M''/M''_{max} and Z''/Z''_{max} relaxation peaks are resolved and separated, indicating that both the long-range conductivity and localized relaxation components are contributing partners in these systems [55]. Furthermore, the relaxation frequencies of M'' and Z'' follow the sequence of scaling of magnitude of relaxation frequencies, i.e., $f_{Z''} \leq f_{M''}$. Therefore, we can safely assume that our plots follow the result $\tau_{\varepsilon''} \geq \tau_{Z''} \geq \tau_{M''}$ [56].

Figure 9a–c represents the frequency-dependent electrical modulus plane plots (M'' vs. M') at different temperatures of LCMO, LCNMO_0.1, 0.9, and LCNMO_0.5, 0.5, respectively. The capacitance of the grain or grain boundary is given by the intercept on the real axis. Two semicircular arcs are observed at low temperatures, implying the contributions of both grain (high-frequency arc) and grain boundary (low-frequency arc). However, when the temperature rises, the semicircular arcs corresponding to the grain are incomplete. This confirms that, at high temperatures, the grain contribution becomes negligible and the grain boundary contribution dominates. Note that the combined plots for the Z'', M'', Z''/Z''_{max}, and M''/M''_{max} vs. frequency plots are providing the knowledge of the nature of movements (short-range or long-range) of charge carriers (See supplementary Fig. 1).

3.5 AC-conductivity

Here, we measured the change in electrical conductivity with frequency to understand the ac and dc contribution of conductivity. Figure 10a–c shows the change in ac conductivity (σ_{ac}) as a function of frequency at different temperatures for the LCMO, LCNMO_0.1, 0.9 and LCNMO_0.5, 0.5 samples. There is a linear increase of σ_{ac} with frequency in the higher frequency region for all samples. However, σ_{ac} is nearly independent of frequency at lower frequencies, which could be associated with the dc contribution. The frequency at which σ_{ac} starts to increase is called the hopping frequency (ω_p) [58]. The following equation usually explains the phenomenon of the conductivity dispersion as [57],

$$\sigma_{ac}(\omega) = \frac{\sigma_s}{1 + \tau^2\omega^2} + \frac{\sigma_\infty \tau^2 \omega^2}{1 + \tau^2\omega^2} + A\omega^s,$$
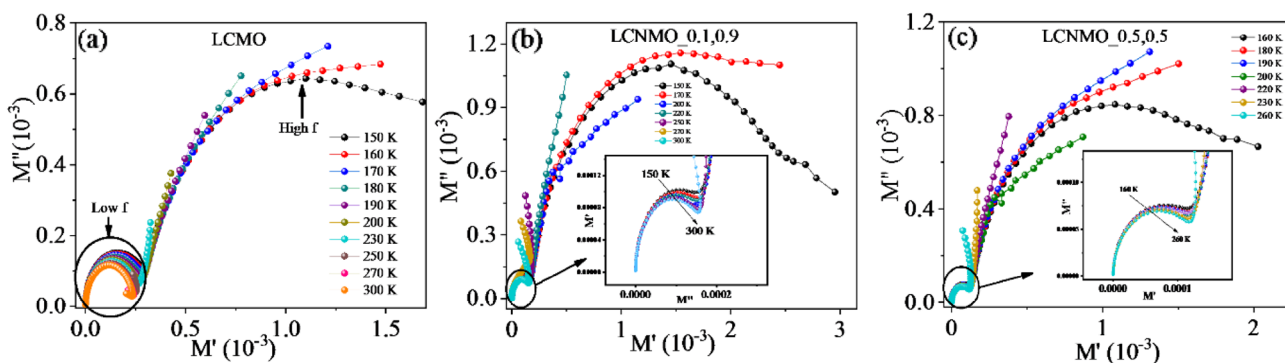

Fig. 9 M'' vs. M' plots for **a** LCMO, **b** LCNMO_0.1, 0.9 and **c** LCNMO_0.5, 0.5 sample
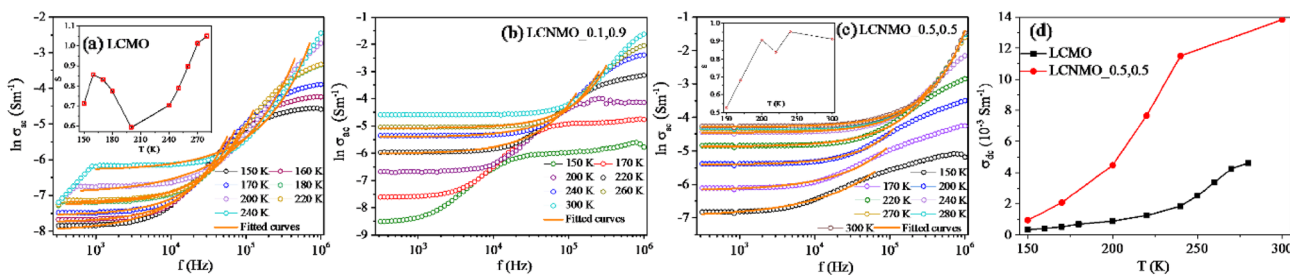

Fig. 10 Frequency-dependent ac conductivity for **a** LCMO, **b** LCNMO_0.1, 0.9 and **c** LCNMO_0.5, 0.5 samples. The insets show the exponent s vs. temperature curves for the respective samples. **d** σ_{dc} vs. temperature curve for LCMO and LCNMO_0.5, 0.5 samples

where σ_s is the conductivity at low frequencies, σ_∞ is an estimate of conductivity at high frequencies, τ represents the characteristic relaxation time; A is a temperature-dependent constant, and $\omega = 2\pi f$ is the angular frequency. The σ_{ac} curves for the studied samples are fitted to the Jonscher's power law [58], expressed as,

$$\sigma_{ac} = \sigma_{dc} + Bf^s,$$

where B is a temperature-dependent pre-factor, s is a unitless exponent function of temperature, and σ_{dc} is related to direct conduction. This law describes the universal dielectric response of any material. It is observed that in case of LCMO, the σ_{ac} curves in the higher temperature range are well fitted with the power-law in the entire frequency range, while the curves < 200 K are fitted well only below 100 kHz. For the sample LCNMO_0.1, 0.9, proper fitting to the power-law is only possible at high temperatures. At low temperatures, step-like features are observed above 10 kHz. This suggests that the universal dielectric response behaviour exists in a very small region, and hence, σ_{ac} curves cannot be fitted well for the LCNMO_0.1, 0.9 sample at low temperatures. For the sample LCNMO_0.5, 0.5, all the curves are fitted well with the power-law at all temperatures. For temperatures below 230 K, the power-law fits well below 100 kHz. The exponent s obtained from the fitting parameter of ln σ_{ac} vs. f for all samples is plotted and shown in the insets of Fig. 10a, c.

There are several proposed mechanisms to understand the relaxation processes in any dielectric material, e.g., Quantum Mechanical Tunneling model (QMT) (s is temperature-independent), Correlated Barrier Hopping model (CBH) (s decreases with increasing temperature), Overlapping Large Polaron Tunneling mechanism (OLPT) (decrease of s with temperature, followed by a minimum; then increase in s with rising temperature), and the Non-overlapping Small Polaron Tunneling (NSPT) model (s increases with increase in temperature) [59–62]. In these dielectric systems, in particular, the LCMO system appears to follow the OLPT mechanism, in which the large polaron wells overlap at two sites by reducing the polaron hopping energy. According to this model, the ac conductivity is given by the equation [63]:

$$\sigma_{ac} = \frac{\pi^4 e^2 (k_B T)^2 [(N(E_F)]^2 \omega R_\omega^4}{12(2\alpha k_B T + \frac{W_{HO} r_p}{R_\omega^2})},$$

where k_B is the Boltzmann constant, T is the temperature, $N(E_F)$ is the density of states at the Fermi level, R_ω is the tunneling distance and α is the spatial extent of polarons. The frequency exponent s is given by the expression:

$$s = 1 - \frac{8\alpha R_\omega + \frac{6\beta W_{HO} r_p}{R_\omega}}{\left[2\alpha R_\omega + \frac{\beta W_{HO} r_p}{R_\omega}\right]^2},$$

where $\beta = \frac{1}{k_B T}$. The polaron hopping energy can be given by the relation $W_H = W_{HO}\left(1 - \frac{r_p}{R}\right)$, where r_p is the polaron radius, R is the intersite separation and $W_{HO} = \frac{e^2}{4\epsilon_p r_p}$. The LCNMO_0.5, 0.5 system probably follows the NSPT mechanism as understood from the s vs. T plot. In this mechanism the ac-conductivity and the exponent s are expressed as [64, 65]

$$\sigma_{ac} = \frac{\pi^2 e^2 (k_B T)\omega[N(E_F)]^2 R_\omega^4}{12\alpha},$$

$$s = 1 + \frac{4k_B T}{W_H - k_B T Ln(\omega \tau_0)},$$

where

$$R_\omega = \frac{1}{2\alpha}\left[Ln\left(\frac{1}{\omega \tau_0}\right) - \left(\frac{W_H}{k_B T}\right)\right]$$

The σ_{dc} values extracted from the power-law fitting are shown in Fig. 10d. The increase in dc-conductivity with temperature further confirms the semiconductor-like nature of our samples.

The plots of ln σ_{ac} vs. 1/T for the samples LCMO, LCNMO_0.1, 0.9 and LCNMO_0.5, 0.5 show a semiconducting nature (not shown). The activation energies of the samples are calculated from the slope of the straight line, using the Arrhenius relation:

$$\sigma_{ac} = \sigma_0 \exp\left(\frac{E_a}{k_B T}\right),$$

where σ_0 is the pre-factor and E_a is the activation energy. The calculated E_a values of all the samples at different frequencies are given in Table 5. For LCNMO_0.1, 0.9 and LCNMO_0.5, 0.5 samples, the activation energies decrease with increasing frequency.

4 Conclusions

High purity double perovskite compounds $La_2Co_{1-x}Ni_xMnO_6$ ($x = 0, 0.1, 0.5$) have been successfully synthesized by the sol–gel method, whereby it is confirmed that the samples crystallize into a monoclinic structure with a space group of $P2_1/n$. The substitution of Ni at the Co site of parent La_2CoMnO_6 leads to higher structural disorder, giving rise to interesting physical properties. An improvement in the

dielectric properties compared to the parent compound is noticed in the $x = 0.1$ and $x = 0.5$ Ni-doped samples where $\varepsilon' \sim 5653$ and ~ 5000 at a frequency of 1 kHz and temperature at 240 K, respectively. All the samples follow the Maxwell–Wagner-type contribution to the variation in permittivity. For samples $x = 0$ and $x = 0.1$, a significant temperature difference between the $\tan \delta$ and ε'' peaks are observed, indicating the absence of permanent dipoles. The samples $x = 0$ and $x = 0.1$ clearly show MD behaviour under 3 T field. All samples exhibit a negative temperature coefficient of resistance. The obtained activation energies related to grain boundary and grain for LCMO, LCNMO_0.1, 0.9 and LCNMO_0.5, 0.5 indicate semiconducting-like behaviour. The Nyquist plots confirm non-Debye type relaxation and follows (RC)(RQC) equivalent circuit diagram. It is confirmed that a similar relaxation mechanism can explain all the relaxation processes at different temperatures. Overlapping Large Polaron Tunneling and Non-overlapping Small Polaron Tunneling models are found to successfully explain the mechanism of charge transport in the parent compound and the $x = 0.5$ system, respectively. We discuss how doping at the $3d$ transition metal ion site in double perovskites plays a crucial role on these interesting properties.

References

1. H.M. Rai, P. Singh, S.K. Saxena, V. Mishra, M.K. Warshi, R. Kumar, P. Rajput, A. Sagdeo, I. Choudhuri, B. Pathak, P.R. Sagdeo, Room-temperature magneto-dielectric effect in $LaGa_{0.7}Fe_{0.3}O_3+\gamma$; origin and impact of excess oxygen. Inorg. Chem. **56**(7), 3809–3819 (2017)

2. S. Mukherjee, S. Chatterjee, S. Rayaprol, S.D. Kaushik, S. Bhattacharya, P.K. Jana, Near room temperature magnetodielectric consequence in (Li, Ti) doped NiO ceramic. J. of Appl. Phys. **119**, 134103 (2016)

3. T. Kimura, T. Goto, H. Shintani, K. Ishizaka, T. Arima, Y. Tokura, Magnetic control of ferroelectric polarization. Nature (London) **426**, 55–58 (2003)

4. T. Kimura, Y. Sekio, H. Nakamura, T. Siegrist, A.P. Ramirez, Cupric oxide as an induced-multiferroic with high-T_C. Nature Mater. **7**, 291 (2008)

5. D. Choudhury, P. Mandal, R. Mathieu, A. Hazarika, A. Sundaresan, S. Rajan, U.V. Waghmare, R. Knut, O. Karis, P. Nordblad, D.D. Sarma, Near-room-temperature colossal magnetodielectricity and multiglass properties in partially disordered La_2NiMnO_6. Phys. Rev. Lett. **108**, 127201 (2012)

6. S. Baidya, T. Saha-Dasgupta, Electronic structure and phonons in La_2CoMnO_6: a ferromagnetic insulator driven by Coulomb-assisted spin-orbit coupling. Phys. Rev. B **84**, 035131 (2011)

7. R.C. Sahoo, S.K. Giri, D. Paladhi, A. Das, T.K. Nath, Influence of magnetic frustration and structural disorder on magnetocaloric effect and magneto-transport properties in $La_{1.5}Ca_{0.5}CoMnO_6$ double perovskite. J. Appl. Phys. **120**, 033906 (2016)

8. K.D. Chandrasekhar, A.K. Das, C. Mitra, A. Venimadhav, The extrinsic origin of the magnetodielectric effect in the double perovskite La_2NiMnO_6. J. Phys. Condens. Matter **24**, 495901 (2012)

9. Z. Weng, J. Qin, A.A. Umar, J. Wang, X. Zhang, H. Wang, X. Cui, X. Li, L. Zheng, Y. Zhan, Lead-free $Cs_2BiAgBr_6$ double perovskite-based humidity sensor with superfast recovery time. Adv. Funct. Mater. **29**, 1902234 (2019)

10. M. Usman, Q. Yan, Recent advancements in crystalline Pb-free halide double perovskites. Curr. Comput.-Aided Drug Des. **10**, 62 (2020)

11. A.M. Idris, T. Liu, J.H. Shah, A.S. Malik, D. Zhao, H. Han, C. Li, Sr_2NiWO_6 double perovskite oxide as a novel visible light responsive water oxidation photocatalyst. ACS Appl. Mater. Interfaces **12**, 25938–25948 (2020)

12. P. Shirazi, M. Rahbar, M. Behpour, M. Ashrafi, La_2MnTiO_6 double perovskite nanostructures as highly efficient visible light photocatalysts. New J. Chem. **44**, 231–238 (2020)

13. J. Krishna Murthy, A. Venimadhav, Metamagnetic behaviour and effect of field cooling on sharp magnetization jumps in multiferroic Y_2CoMnO_6. Eur. Phy. Lett. **108**, 27013 (2014)

14. R.C. Sahoo, S. Das, T.K. Nath, Size modulated Griffiths phase and spin dynamics in double perovskite $Sm_{1.5}Ca_{0.5}CoMnO_6$. J. Magn. Magn. Mater. **460**, 409–417 (2018)

15. R.P. Madhogaria, R. Da, E.M. Clements, V. Kalappattil, N.S. Bingham, M.H. Phan, H. Srikanth, Effect of antiphase boundaries on the magnetic properties of La_2CoMnO_6. AIP Adv **9**, 035142 (2019)

16. R. Egoavil, S. Hühn, M. Jungbauer, N. Gauquelin, A. Béché, G. Van Tendeloo, J. Verbeeck, V. Moshnyaga, Phase problem in the B-site ordering of La_2CoMnO_6: impact on structure and magnetism. Nanoscale **7**, 9835–9843 (2015)

17. R.N. Mahato, K. Sethupathi, V. Sankaranarayanan, Colossal magnetoresistance in the double perovskite oxide La_2CoMnO_6. J. Appl. Phys. **107**, 09D714 (2010)

18. R. I. Dass and J. B. Goodenough, Multiple magnetic phases of $La_2CoMnO_{6-\delta}$ ($0 < \sim \delta < \sim 0.05$). Phys. Rev. B **67**, 014401 (2003)

19. M.P. Singh, K.D. Truong, P. Fournier, Magnetodielectric effect in double perovskite La_2CoMnO_6 thin films. Appl. Phys. Lett. **91**, 042504 (2007)

20. Y.Q. Lin, X.M. Chen, Dielectric, ferromagnetic characteristics, and room-temperature magnetodielectric effects in double perovskite La_2CoMnO_6 ceramics. J. Am. Ceram. Soc. **94**, 782 (2011)

21. R. X. Silva, A. S. Menezes, R. M. Almeida, R. L. Moreira, R. Paniago, X. Marti, H. Reichlova, M. Maryško, M. Vinicius dos S. Rezende, C. W. A. Paschoa, Structural order, magnetic and intrinsic dielectric properties of magnetoelectric La_2CoMnO_6. J. Alloys Compd. **661**, 541-552 (2016)

22. S. Das, R.C. Sahoo, T.K. Nath, Investigation of room temperature multiferroic properties in sol-gel derived gadolinium, cobalt doped $BiFeO_3$ nanoceramics. J. Appl. Phys. **127**, 054101 (2020)

23. N. Kim, S. Cho, S.H. Park, Y.J. Lee, R.A. Afzal, J. Yoo, Y. Seo, Y.J. Lee, J. Park, B-site doping effects of $NdBa_{0.75}Ca_{0.25}Co_2O_5+\delta$ double perovskite catalysts for oxygen evolution and reduction reactions. J. Mater. Chem. A **6**, 17807–17818 (2018)

24. L. Chen, C. Yuan, J. Xue, J. Wang, B-site ordering and magnetic behaviours in Ni-doped double perovskite Sr_2FeMoO_6. J. Phys. D Appl. Phys. **38**, 4003 (2005)

25. H.T. Handal, H.A. Mousa, S.M. Yakout, W. Sharmoukh, V. Thangadurai, Effect of Mn and Ni-doping on structure, photoluminescence and magnetic properties of perovskite-type $BaSn_{0.99}Gd_{0.01}O_3$. J. Magn. Magn. Mater. **498**, 165946 (2020)

26. S. Fei Liu, Y. Jun Wu, J. Li, X. Ming Chen, Effects of oxygen vacancies on dielectric, electrical, and ferroelectric properties of $Ba_4Nd_2Fe_2Nb_8O_{30}$ ceramics. Appl. Phys. Lett. **104**, 082912 (2014)

27. R. Tang, C. Jiang, W. Qian, J. Jian, X. Zhang, H. Wang, H. Yang, Dielectric relaxation, resonance and scaling behaviors in $Sr_3Co_2Fe_{24}O_{41}$ hexaferrite. Sci. Rep. **5**, 13645 (2015)

28. V. Petkov, Y. Peng, G. Williams, B. Huang, D. Tomalia, Y. Ren, Structure of gold nanoparticles suspended in water studied by x-ray diffraction and computer simulations. Phys. Rev. B **72**, 195402 (2005)

29. E. Enriquez, A. Chen, Z. Harrell, X. Lu, P. Dowden, N. Koskelo, M. Janoschek, C. Chen, Q. Jia, Oxygen vacancy-driven evolution of structural and electrical properties in $SrFeO_{3-\delta}$ thin films and a method of stabilization. Appl. Phys. Lett. **109**, 141906 (2016)

30. D. Serrate, J.M.D. Teresa, P.A. Algarabel, C. Marquina, J. Blasco, M.R. Ibarra, J. Galibert, Magnetoelastic coupling in $Sr_2(Fe_{1-x}Cr_x)ReO_6$ double perovskites. J. Phys. Cond. Matt. **19**, 436226 (2007)

31. Z. Songand, Q. Liu, Tolerance factor, phase stability and order–disorder of the pyrochlore structure. Inorg. Chem. Front. **7**, 1583 (2020)

32. G. Popov, M. Greenblatt, M. Croft, Large effects of A-site average cation size on the properties of the double perovskites $Ba_{2-x}Sr_xMnReO_6$: a d5–d1 system. Phys. Rev. B **67**, 024406 (2003)

33. S. Halder, S. Bhuyan, R.N.P. Choudhary, Structural, dielectric and electrical characteristics of lead-free electro-ceramic: $Bi(Ni_{2/3}Ta_{1/3})O_3$. Eng. Sci. Technol. **22**, 376–384 (2019)

34. S. Hunpratub, P. Thongbai, T. Yamwong, R. Yimnirun, S. Maensiri, Dielectric relaxations and dielectric response in multiferroic $BiFeO_3$ ceramics. Appl. Phys. Lett. **94**, 062904 (2009)

35. W.N. Su, D.H. Wang, Q.Q. Cao, Z.D. Han, J. Yin, J.R. Zhang, Y.W. Du, Large polarization and enhanced magnetic properties in $BiFeO_3$ ceramic prepared by high-pressure synthesis. Appl. Phys. Lett. **91**, 092905 (2007)

36. X. Chen, R. Yang, J. Zhou, X. Chen, Q. Jiang, P. Liu, Dielectric and magnetic properties of multiferroic $BiFeO_3$ ceramics sintered with the powders prepared by hydrothermal method. Solid State Sci. **19**, 117–121 (2013)

37. M.M. Ahmad, Giant dielectric constant in $CaCu_3Ti_4O_{12}$ nanoceramics. Appl. Phys. Lett. **102**, 232908 (2013)

38. P. Lunkenheimer, S. Krohns, S. Riegg, S.G. Ebbinghaus, A. Reller, A. Loidl, Colossal dielectric constants in transition-metal oxides. Eur. Phys. J. Spec. Top. **180**, 61–89 (2009)

39. F. Schrettle, P. Lunkenheimer, J. Hemberger, V.Y. Ivanov, A.A. Mukhin, A.M. Balbashov, A. Loidl, Relaxations as key to the magnetocapacitive effects in the perovskite manganites. Phys. Rev. Lett. **102**, 207208 (2009)

40. S. Kamba, D. Nuzhnyy, M. Savinov, J. Šebek, J. Petzelt, J. Prokleška, R. Haumont, J. Kreisel, Infrared and terahertz studies of polar phonons and magnetodielectric effect in multiferroic $BiFeO_3$ ceramics. Phys. Rev. B **75**, 024403 (2007)

41. C. Rayssi, S.E. Kossia, J. Dhahri, K. Khirounib, Frequency and temperature-dependence of dielectric permittivity and electric modulus studies of the solid solution $Ca_{0.85}Er_{0.1}Ti_{1-x}Co_{4x/3}O_3$ ($0 \leq x \leq 0.1$). RSC Adv. **8**, 17139–17150 (2018)

42. C.C. Wang, M.N. Zhang, K.B. Xu, G.J. Wang, Oxygen-vacancy-related dielectric relaxations in $SrTiO_3$ at high temperatures. J. Appl. Phys. **112**, 034109 (2012)

43. M. Li, A. Feteira, D.C. Sinclair, Relaxor ferroelectric-like high effective permittivity in leaky dielectrics/oxide semiconductors induced by electrode effects: a case study of CuO ceramics. J. Appl. Phys. **105**, 114109 (2009)

44. S. Raut, P.D. Babu, R.K. Sharma, R. Pattanayak, S. Panigrahi, Grain boundary-dominated electrical conduction and anomalous optical-phonon behaviour near the Neel temperature in $YFeO_3$ ceramics. J. Appl. Phys. **123**, 174101 (2018)

45. S. Das, R.C. Sahoo, K.P. Bera, T.K. Nath, Doping effect on ferromagnetism, ferroelectricity and dielectric constant in sol–gel derived $Bi_{1-x}Nd_xFe_{1-y}Co_yO_3$ nanoceramics. J. Magn. Magn. Mater. **451**, 226–234 (2018)

46. J. Krishna Murthy, A. Venimadhav, Magnetodielectric behavior in La_2CoMnO_6 nanoparticles. J. Appl. Phys. **111**, 024102 (2012)

47. N.S. Rogado, J. Li, A.W. Sleight, M.A. Subramaniam, Magnetocapacitance and magnetoresistance near room temperature in a ferromagnetic semiconductor: La_2NiMnO_6. Adv. Mater. **17**, 2225–2227 (2005)

48. J.R. Mac Donald, *Impedance spectroscopy* (John Wiley and Sons, Hoboken, 1987)

49. B. Tiwari, R.N.P. Choudhary, Complex impedance spectroscopic analysis of Mn-modified $Pb(Zr_{0.65}Ti_{0.35})O_3$ electroceramics. J. Phys. Chem. Solids **69**, 2852 (2008)

50. B. Behera, P. Nayaka, R.N.P. Choudhary, Study of complex impedance spectroscopic properties of $LiBa_2Nb_5O_{15}$ ceramics. Mater. Chem. Phys. **106**, 193–197 (2007)

51. D. Triyono, C.A. Kafa, H. Laysandra, Effect of Sr-substitution on the structural and dielectric properties of $LaFeO_3$ perovskite materials. J. Adv. Dielectr. **08**, 1850036 (2018)

52. M. Idrees, M. Nadeem, M. Mahmood, M. Atif, K.H. Chae, M.M. Hassan, Impedance spectroscopic investigation of delocalization effects of disorder induced by Ni doping in $LaFeO_3$. J. Phys. D: App. Phys. **44**, 105401 (2011)

53. O. Bidault, M. Maglione, M. Actis, M. Kchikech, B. Salce, Polaronic relaxation in perovskites. Phys. Rev. B **52**, 4191 (1995)

54. V.F. Lvovic, *Impedance spectroscopy, applications to electrochemical and dielectric phenomena* (John Wiley and Sons, Hoboken, 2012)

55. S. Thakur, R. Rai, I. Bdikin, M.A. Valentec, Impedance and modulus spectroscopy characterization of Tb modified $Bi_{0.8}A_{0.1}Pb_{0.1}Fe_{0.9}Ti_{0.1}O_3$ ceramics. Mater. Res. **19**(1), 1–8 (2016)

56. R. Gerhardt, Impedance and dielectric spectroscopy revisited: Distinguishing localized relaxation from long-range conductivity. J. Phys. Chem. Solids **55**, 1491 (1994)

57. M. Sassi, A. Oueslati, M. Gargouri, Ionic ac and dc conductivities of $NaCrP_2O_7$ compound. Appl. Phys. A **119**, 763 (2015)

58. E. Sentürk, Y. Koseoglu, T. Sasmaz, F. Alan, M. Tan, RC circuit and conductivity properties of $Mn_{0.6}Co_{0.4}Fe_2O_4$ nanocomposite synthesized by hydrothermal method. J. Alloys. Compd. **578**, 90 (2013)

59. A. Ghosh, D. Chakravorty, AC conduction in semiconducting $Cu_O \cdot Bi_2O_3 \cdot P_2O_5$ glasses. J. Phys. Condens. Matter **2**, 5365 (1990)

60. X. Le Cleac'h, Lois de variations et ordre de grandeur de la conductivité alternative des chalcogénures massifs non cristallins. J. Phys. **40**, 417 (1979)

61. G.E. Pike, AC conductivity of scandium oxide and a new hopping model for conductivity. Phys. Rev. B **6**, 1572 (1972)

62. S.R. Elliott, A theory of a.c. conduction in chalcogenide glasses. Philos. Mag. B **36**, 1291 (1977)

63. I.G. Austin, N.F. Mott, Polarons in crystalline and non-crystalline materials. Adv. Phys. **18**, 41 (1969)

64. S.R. Elliott, A.C. conduction in amorphous chalcogenide and pnictide semiconductors. Adv. Phys. **36**, 135 (1987)

65. A. Kahouli, A. Sylvestre, F. Jomni, B. Yangui, J. Legrand, Experimental and theoretical study of AC electrical conduction mechanisms of semicrystalline parylene C thin films. J. Phys. Chem. A **116**, 1051–1058 (2012)